

Analyst

Accepted Manuscript



This is an *Accepted Manuscript*, which has been through the Royal Society of Chemistry peer review process and has been accepted for publication.

Accepted Manuscripts are published online shortly after acceptance, before technical editing, formatting and proof reading. Using this free service, authors can make their results available to the community, in citable form, before we publish the edited article. We will replace this *Accepted Manuscript* with the edited and formatted *Advance Article* as soon as it is available.

You can find more information about *Accepted Manuscripts* in the [Information for Authors](#).

Please note that technical editing may introduce minor changes to the text and/or graphics, which may alter content. The journal's standard [Terms & Conditions](#) and the [Ethical guidelines](#) still apply. In no event shall the Royal Society of Chemistry be held responsible for any errors or omissions in this *Accepted Manuscript* or any consequences arising from the use of any information it contains.



Analyst

PAPER

Reduced Graphene Oxide-Nickel Nanoparticles/Biopolymer Composite Films for Sub-Millimolar Detection of Glucose†

Rahul Krishna,^{a,b,c} José M. Campiña,^a Paula M. V. Fernandes,^a João Ventura,^c Elby Titus,^b and António F. Silva^a

Received 00th January 20xx,
Accepted 00th January 20xx

DOI: 10.1039/x0xx00000x

www.rsc.org/

Hybrid conjugates of graphene with metallic/semiconducting nanostructures could improve the sensitivity of electrochemical sensors due to their combination of well-balanced electrical/electrocatalytic properties and superior surface-to-volume ratio. In this work, the synthesis and physical characterization of a hybrid conjugate of reduced graphene oxide and nickel nanoparticles (rGO-Ni NPs) is presented. The conjugate was further deposited onto a glassy carbon electrode as a nanocomposite film of chitosan and glucose oxidase. The electrochemical response and morphology of the films were investigated by SEM, CV, and EIS, and their application as a glucose biosensor were explored for the first time in proof-of-concept tests. The low operating potential along with the good linearity and sensitivity (up to 129 $\mu\text{A}\cdot\text{cm}^{-2}\cdot\text{mM}^{-1}$) found in the sub-millimolar range, suggest potential applications in the self-management of hypoglycemia from blood samples or in the development of non-invasive assays for body fluids such as saliva, tears, or breath.

Introduction

The disorders of carbohydrate metabolism are often regarded as the pandemics of the modern times. Only *Diabetes Mellitus* affected to 2.8% of the world population in 2000 (figures which could double by 2030).¹ To date, the self-management of blood glucose levels has been the best proven approach to delay clinical complications.² In this sense, different generations of glucose sensors have been commercially available since the 60s. Biosensors, which take benefit from the high specificity of enzymatic processes (catalytic or enzymatic biosensors: e.g. glucose sensors³) and molecular recognition phenomena (affinity biosensors: e.g. immunosensors,⁴ DNA/RNA aptasensors,⁵ or molecularly imprinted polymers⁶), have expanded from healthcare to environmental monitoring, food safety, homeland security, etc; reaching a predicted market value of \$20 billion by 2020.⁷

Electrochemical sensors present inherent advantages such as good sensitivity, rapid and reliable response, and no need of laborious sample pretreatment or labeling. Furthermore, low-cost miniaturized chips and portable hand-held electrochemical readers put this technology ahead of their

competitors for the development of wearable analytical tools that enable the self-management of different conditions.^{5,8} Despite their excellent selectivity, the sensitivity of biosensors is often limited by:

- (a) Low coverage of biomolecules (enzymes, antibodies, and so on) immobilized on a 2D supports.
- (b) Poor conformational stability of surface-attached biomolecules.
- (c) Insulating or semiconducting nature of the most common supports (polymers, hydrogels, inorganic scaffolds, etc).

Nanotechnology has shrunk the dimensions of the main sensor elements for enhanced signal-to-noise (S/N) ratios. Nanostructured transducers and/or supporting matrices, exhibit much higher surface-to-volume ratios to improve the density of attached biomolecules. Regarding point (b), covalent immobilization typically leads to low coverage and/or reduced biological activity (due to the conformational changes triggered by the coupling chemistries). Oppositely, passive adsorption improves coverage but makes it harder to control molecular orientation and the organization of the layers. In parallel, protein unfolding is favored on many surfaces which further limits the activity of the attached biomolecules.⁹

Conductivity enhancers such as redox mediators,¹⁰ conductive polymers,¹¹ metal nanoparticles (MNPs),¹² and carbon nanomaterials, have been addressed to solve point (c). In this sense, carbon nanotubes (CNTs) allowed the direct electron transfer (ET) between redox enzymes and electrodes.¹³ More recently, graphene (an one atom thick 2D sheet of honeycomb carbon easily prepared from graphite¹⁴ or by vapor deposition¹⁵) has also been explored.^{16,17} Compared to CNTs, graphene has larger surface area, fewer impurities,

^a Centre for Research in Chemistry of The University of Porto (CIQUP), Dept. of Chemistry and Biochemistry, Faculty of Sciences, Rua do Campo Alegre s/n, 4169-007 Porto, Portugal.

^b Centre for Mechanical Technology and Automation (TEMA), Dept. of Mechanical Engineering, University of Aveiro, 3810-193, Aveiro, Portugal.

^c IFIMUP-IN and Faculty of Sciences, University of Porto, Rua do Campo Alegre s/n, 4169-007 Porto, Portugal.

† Electronic Supplementary Information (ESI) available: Equivalent circuit description; Glucose adsorption on bare GCE; Energy dispersive analysis; Biosensor reproducibility; Amperometric calibration; Stability and durability tests; Interference tests. See DOI: 10.1039/x0xx00000x

and superior mechanical and electrical properties.^{14,18} Indeed, water-processable chemically modified forms of graphene, e.g. graphene oxide (GO), are obtained in bulk quantities by functionalization and exfoliation of graphite.

GO has been explored as a membrane material¹⁹ and a mechanical reinforcer.²⁰ Despite its poor electron conductivity, it presents good electrocatalytic properties²¹ due to a high density of functional groups and structural defects.²² After reduction to rGO, the conductivity is partially restored but, unavoidably, certain amount of functional groups and defects, remain in the structure. Therefore, rGO is a better balanced material for electrochemical applications. More recently, hybrid conjugates of rGO and metallic/semiconducting NPs (rGO-MNPs/SNPs) have been explored for energy storage, catalysis, analysis, and so on.²³⁻⁴² So far the most investigated conjugates in electroanalytical applications include MNPs of Au,²³⁻²⁵ Cu,^{26,27} and Pt.²⁸ While the use of Ni NPs may bring similar advantages in terms of surface-to-volume area, Ni is a cheaper and less toxic metal than the previous. Despite these advantages, the rGO-Ni hybrid conjugate has been only explored in a handful of non-enzymatic sensors for the detection of glucose (and other carbohydrates)³⁷⁻⁴¹ and, to our best knowledge, no glucose biosensor based on this enhancer has been demonstrated to date.

In this paper, the synthesis and characterization of a rGO-Ni NPs conjugate and the preparation of nanocomposite films with chitosan (a deacetylated derivative of the abundant chitin polysaccharide which is used in graphene composites^{23,28,43} due to its excellent film forming abilities and biocompatibility^{44,45}) and glucose oxidase (GOx), is described. Applications as a glucose biosensor were explored in proof-of-concept assays mediated by $[\text{Fe}(\text{CN})_6]^{3-/4-}$ redox probes.^{46,47} This approach brings the advantages of the enhanced surface area and balanced electrical/electrochemical properties of the rGO-Ni NPs conjugate, the excellent biocompatibility and enhanced density of enzyme molecules accommodated in the chitosan scaffold, and the excellent selectivity of GOx.

Experimental

Synthesis of the rGO-Ni NPs Conjugate

GO was synthesized from graphite powder through a modified Hummers method.⁴⁸ Hybrid sheets of rGO-Ni NPs were grown *in situ* as summarized in Scheme 1a. In first place, 100 mL of GO aqueous dispersion ($1 \text{ mg}\cdot\text{mL}^{-1}$) were placed in a 4-neck round bottom flask and 600 mg of nickel chloride hexahydrate ($\text{NiCl}_2\cdot 6\text{H}_2\text{O}$, >98%, Sigma-Aldrich) were added. The temperature was gradually increased to 85°C and, then, 18 mL of hydrazine hydrate (N_2H_4 , 64-65%, reagent grade, Sigma) were slowly poured. After 25 min stirring in Ar atmosphere, 450 mg of sodium borohydride (NaBH_4 , 98%, Sigma) were very slowly added. Finally, 25 mL of 1 M sodium hydroxide (NaOH) were added and the mixture was stirred for another 150 min. The product was filtered, washed with ethanol and doubled-distilled water, and vacuum-dried at 100°C for 3 h.

Preparation of the rGO-Ni/Chit95/GOx Films

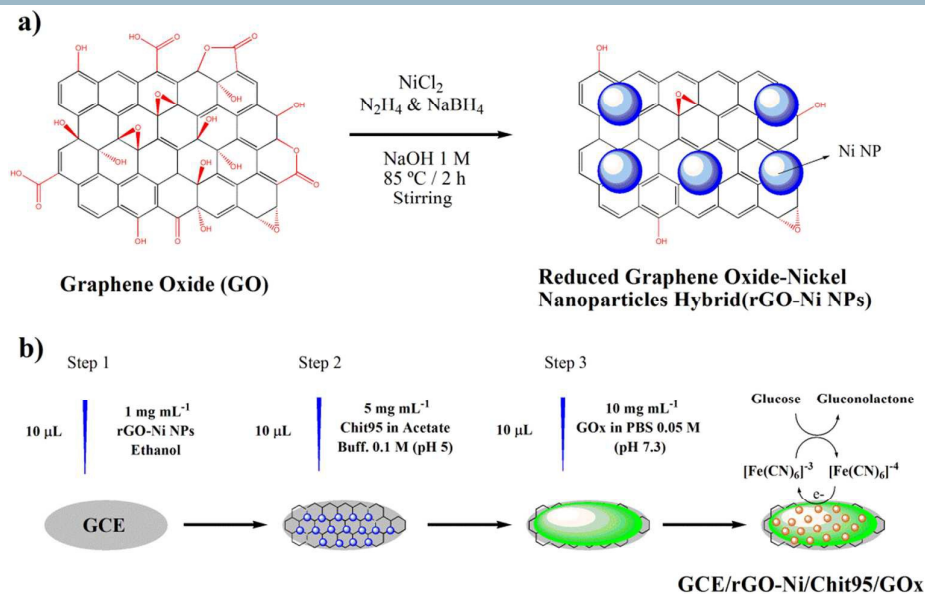
The rGO-Ni/Chit95/GOx composite films were deposited onto a glassy carbon electrode (GCE, Metrohm, 6.1204.300, area: 0.06 cm^2) by sequential drop-casting. Previously, the GCE was polished with $0.3 \mu\text{m}$ Alumina slurry (Buehler Micropolish II) and consecutively washed in water, ethanol, and acetone under sonication. Cyclic voltammetry (CV) in H_2SO_4 0.5 M was used to assess the cleanliness of the electrode. Then, it was modified in three sequential steps (Scheme 1b). In the first, 10 μL of a $1 \text{ mg}\cdot\text{mL}^{-1}$ rGO-Ni NPs dispersion in ethanol were spread on it and air dried. Afterwards, 10 μL of a $5 \text{ mg}\cdot\text{mL}^{-1}$ dispersion of chitosan (deacetylated to a degree of DD=95%, average molecular mass: 150-200 kDa, Primex, Iceland; hereinafter referred to as Chit95) in acetate buffer 0.1 M (pH 5; AB) were casted. Once dried, 10 μL of a $10 \text{ mg}\cdot\text{mL}^{-1}$ solution of glucose oxidase (from *Aspergillus Niger*, Fluka; GOx) in 0.05 M phosphate buffer + 0.15 M NaCl (pH 7.3; PBS) were dropped. To enhance the enzyme loading, GOx was casted twice. AB and PBS solutions were prepared in ultrapure water from a Milli-RO 3 Plus system ($18.2 \text{ M}\Omega\cdot\text{cm}$ resistivity). When not in use, the stock solutions and modified electrodes were stored at 4°C . Films of Chit95, GOx, Chit95/GOx, rGO-Ni NPs, and rGO-Ni/Chit95 were also prepared, by combinations of the previous steps, for the sake of comparison.

Methods

Characterization of the Conjugate. The phase purity and crystalline structure were assessed by X-ray diffraction (XRD, $\text{Cu K}\alpha$ radiation, $\lambda=0.15414 \text{ nm}$; $0.02^\circ\cdot\text{min}^{-1}$). Attenuated total reflectance fourier-transformed infrared (ATR-FTIR) spectra were recorded in a Bruker Tensor 27. X-ray photoelectron spectroscopy (XPS) was performed in an ESCALAB 200A spectrometer (VG Scientific, UK) equipped with an achromatic Al ($\text{K}\alpha$) X-ray source of 15 kV (300 W) and operated in CAE mode (20 eV pass energy). The analysis of the spectra was done with the XPS Peak 4.1 software (Gaussian-Lorentzian peak shape). For deconvolution, a non-linear least squares fitting routine (plus Shirley-type background subtraction). Conventional high-resolution transmission electron microscopy (HRTEM, LaB₆) was used to investigate the crystallinity and quality of the conjugate.

Characterization of the Composites. Field effect scanning electron microscopy (FESEM) images were taken for the rGO-Ni NPs conjugate and the composite films in a FEI Quanta 400FEG Genesis X4M Microscope (CEMUP, Centro de Materiais da Universidade do Porto) with Energy-dispersive X-Ray Analysis (EDX). The preparation of the films was followed by cyclic voltammetry (CV) and electrochemical impedance spectroscopy (EIS) in pure PBS and PBS + 2 mM $\text{K}_4[\text{Fe}(\text{CN})_6]\cdot 3\text{H}_2\text{O}$ + 2 mM $\text{K}_3[\text{Fe}(\text{CN})_6]$ (Fluka) using a Voltalab PGZ301 potentiostat (Radiometer Analytical). Pt and Ag wires were used as counter and pseudo-reference electrodes, respectively.

CVs were acquired in the range $-0.3/+0.6 \text{ V}$ at $0.05 \text{ V}\cdot\text{s}^{-1}$. The $[\text{Fe}(\text{CN})_6]^{4-/3-}$ probes allowed for the internal calibration of the pseudo-reference electrode and good agreement was found between the half-wave potential of the probes ($E_{1/2}$) and



Scheme 1. (a) Modified Hummers method followed to synthesize the rGO-Ni NPs hybrid conjugate. (b) Artistic illustration showing the different steps applied for the preparation of a rGO-Ni/Chit95/GOx nanocomposite film onto a clean GCE.

its tabulated standard potential (E°) vs the Ag/AgCl/NaCl reference. Impedance spectra were taken at $E_{1/2}$ (+0.15 V) using a sine wave of 10 mV amplitude. The frequency was decreased from 10^4 to 10^{-1} Hz. Unless otherwise stated, the spectra were fitted to a R_1QR_2W Randles-type equivalent circuit (described in Section S1†). The electrolyte was purged with N_2 for 10–15 min before measurements.

Electroanalytical Studies. GOx-modified electrodes (GCE/GOx, GCE/Chit95/GOx, and GCE/rGO-Ni/Chit95/GOx) were interrogated in PBS + 2 mM $[\text{Fe}(\text{CN})_6]^{3-/4-}$ + 1 mM D-glucose (Merck). The response and analytical performance of GCE/rGO-Ni/Chit95/GOx was further investigated within a range of glucose concentrations ($[\text{G}]$) between 25 μM and 12 mM. CVs and EIS were collected for three electrode replicas.

Results and Discussion

Characterization of the rGO-Ni NPs Conjugate

The XRD patterns of GO and rGO-Ni NPs are shown in Fig 1 (panel a). For GO, a virtually flat diffractogram dominated by one single spike at $2\theta=11^\circ$, which is typically ascribed to its (001) basal plane,^{49,50} was registered (green curve). The d-spacing was $d_{001}=0.81$ nm which agrees well with the interlayer distance in GO (typical values for graphite flakes are ≈ 0.33 nm). Such an increase in the distance between graphitic sheets indicates a successful introduction of functional groups and solvent molecules. In big contrast, the diffractogram of rGO-Ni NPs featured a series of bands at $2\theta > 20^\circ$ (blue curve).

The small band at 23° is due to the (002) crystallographic plane of rGO.⁴⁹ From its low intensity, it is strongly suggested that rGO sheets are covered by a different material.

The rest of peaks matched well the typical pattern of Ni crystals with face centered cubic structure (fcc) [JCPDS card No. 04-0850]. In this sense, the intense band at 44.4° (ascribed to diffraction by Ni (111) facets) confirms the good crystallinity of the grown NPs. Deeper insights on the composition of the hybrid were obtained by ATR-FTIRS (Fig 1b). The spectrum of GO exhibited a series of bands (green curve). While the main of these peaks, registered at 1625 cm^{-1} , involves a variety of possible vibrations (asymmetric stretching in deprotonated carboxyls, $\nu_{\text{COO,AS}}$; stretching in ketones, $\nu_{\text{C=O}}$,⁵¹ or O-H bending in adsorbed H_2O); the peak at 1730 cm^{-1} is precisely ascribed to symmetric carbonyl stretching in edge carboxyl groups, ν_{COOH} .

Other bands were also found at 1220 cm^{-1} (C-O-C asymmetric stretching in epoxides), 1415 cm^{-1} (combined carbonyl stretching and in-plane C-O-H bending in protonated carboxyls, $\nu_{\text{C-OH}}$), and the small shoulder at 1810 cm^{-1} (carbonyl stretching in chloride acids).^{42,49-52} For rGO-Ni, significant absorption only took place at 1595 cm^{-1} which may involve: (1) largely restored sp^2 -hybridized C=C aromatic vibrations,⁵² (2) residual carboxyl or ketone groups (literature has shown that a complete reduction of GO is difficult to achieve even by high-temperature annealing⁵²), or (3) adsorbed H_2O . In summary, not only most of the vibrations related to oxygen-based functional groups vanished from the spectrum but no new

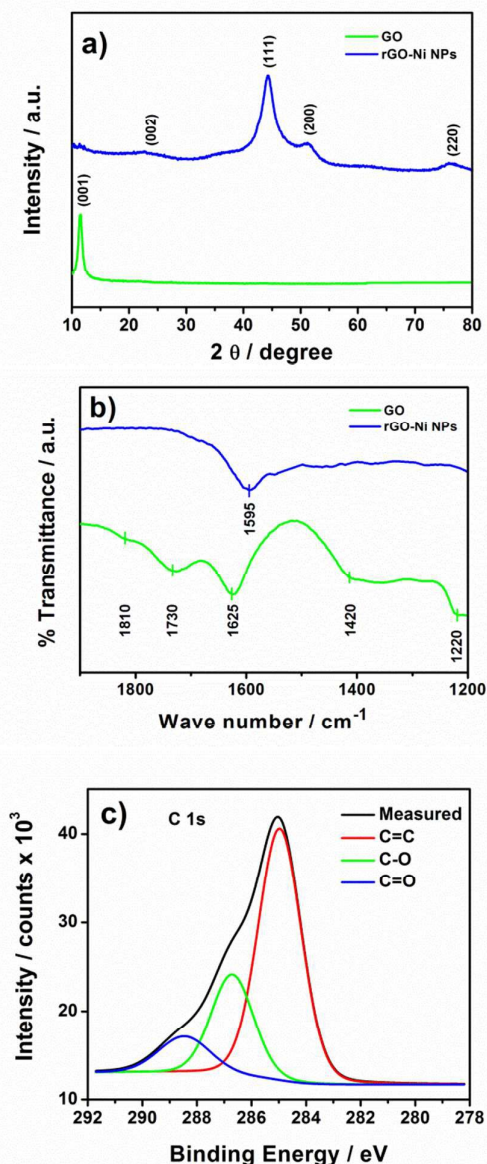


Figure 1. XRD patterns (a) and ATR-FTIR spectra (b) obtained for GO (green curves) and rGO-Ni NPs (blue) powder samples. (c) The C 1s XPS spectrum measured for rGO-Ni NPs (black) and its corresponding de-convolution curves (colored).

peaks accounting for distinct functional groups were also observed. These results strongly support that, through the described method, a high degree of reduction of the original GO sheets to rGO was achieved.

This view was additionally confirmed by XPS. Fig 1c depicts the de-convoluted C 1s core level spectrum of rGO-Ni NPs. While the major peak at 284.9 eV is attributed to the sp^2 C=C bond (graphitic carbon bonding), the peaks at 286.6 eV and 288.5 eV are assigned to carbon-attached remaining oxygen functionalities (C-O and C=O, respectively). The morphology of the conjugate was inspected by SEM (Fig 2a). The image

displays bright spherical clusters of particles with size below the micron which seem deposited onto a surface apparently covered by 2D sheets of graphene. More details were obtained with the HRTEM technique. Fig 2b displays a 2D sheet of rGO decorated with a homogeneous distribution of NPs (5-10 nm size). Despite the good degree of isolation of the NPs in this sample, clusters of about 3-5 NPs (size: 15-20 nm) were also found in this image.

Fabrication of the Composite Films

The buildup process was followed by electrochemical measurements in PBS (Fig 3). Panel a presents the CVs registered for bare GCE, GCE/GOx, GCE/Chit95, GCE/Chit95/GOx, and GCE/rGO-Ni. Interestingly the capacitive current exhibited by the bare GCE (black solid curve) was significantly blocked after adsorption of GOx (red solid curve). The hypothetical unfolding of GOx molecules on GCE to form a hydrophobic blocking layer, would result in a significant reduction of the electrode capacitance. Hence, the evidence points to a poor conformational stability of GOx onto glassy carbon (GC). In great contrast, the capacitive current of GCE/Chit95 (green solid curve) overtook that exhibited by the bare GCE.

The pK_a of $-\text{NH}_2$ groups in chitosan falls around 6.5. Hence, chitosan exhibits positive charge at pHs ranging from acidic to neutral. Due to the high DD of Chit95, and because it was deposited since AB pH 5 (i.e. the pH at the electrode surface may be slightly inferior to that at the electrolyte),⁵³ it would not be surprising that it remained partially protonated under the working conditions (pH 7.3). In such a case, solution anions (and their associated water molecules) would diffuse within the biopolymer matrix to keep the electroneutrality. As a consequence, the capacitance of the electrode should increase as it is reflected in the recorded CV.

Contrary to behavior of GCE/GOx, the CV of GCE/Chit95/GOx (green dashed line) presented negligible changes compared to GCE/Chit95. This may be due to: (1) the GCE surface is densely covered by Chit95 and no direct adsorption of GOx onto the GCE surface occurs, or (2) the biopolymer surface area is much higher than that for uncovered GCE so that the impact of GOx unfolding on the average electrochemical response is nearly negligible. In any case, the result confirms an improved stability of GOx when supported by Chit95. For GCE/rGO-Ni (blue solid line), a large increase of the non-faradaic current was noticed throughout the whole potential range. Moreover, a pair of sharp peaks were identified at +0.07 and -0.27 V.

The enlarged double layer is typical of graphene-modified electrodes (and attributed to its high surface-to-volume ratio and the consequent increase in the amount of storable interfacial charge). G. Chen *et al.* reported an analogous pair of peaks for a magnetically assembled rGO-Ni NPs electrode.³⁸ Despite differences in CV-shape and peak potentials (which may originate from the different synthesis and electrode preparation), a broad peak-to-peak potential separation ($\Delta E_p \geq 320$ mV) was found in both cases. Chen assigned the peaks to the electroactivity of the $\text{NiOOH}/\text{Ni}(\text{OH})_2$ redox pair. Given the

Analyst

PAPER

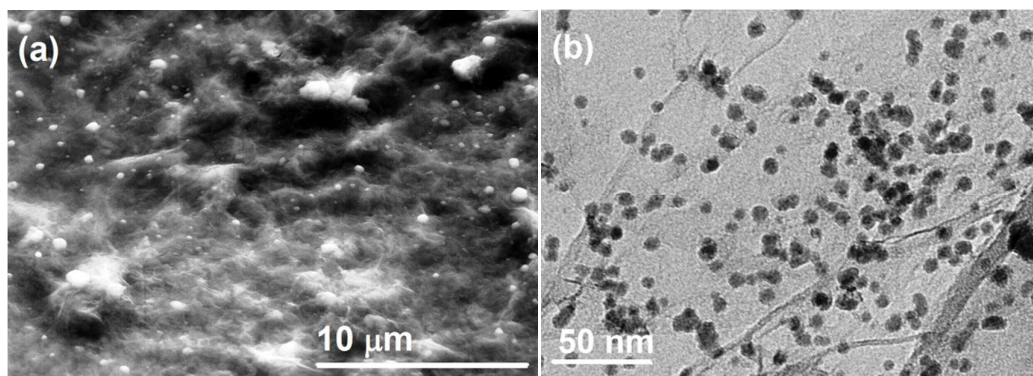


Figure 2. (a) SEM and (b) HRTEM images taken for the rGO-Ni NPs powder.

absence of redox probes in our experiments, the faradaic peaks in Fig 3a must be ascribed to the Ni NPs species in the hybrid conjugate. Further coating of the GCE/rGO-Ni electrode (black curve in Fig 3b) with Chit95 caused a very slight decrease of the non-faradaic currents (red curve). However, the subsequent deposition of GOx (blue curve) resulted in an important blockage of the faradaic processes. These results evidence a continuous passivation of the Ni NPs surface after deposition of the biopolymer and the enzyme layers.

Structure and Composition

The morphology of the rGO-Ni/Chit95/GOx films was inspected by FESEM. Fig 4a shows a wide view at the borders of the electrode surface and its housing. The GC surface is covered by a thick, smooth, and uniform film which looks like a hydrogel. Over the electrode housing, a cracked region revealed the polymeric structure of polyether ether ketone (PEEK) below the detached film. At the right end of the crack, the film was twisted so that its entire cross-section was exposed. From this particular feature, the film thickness could be roughly estimated in 3-4 μm . Some microns to the left, a bunch of graphene sheets appeared wrapped in the film (see a higher magnification image in the red inset).

Fig 4b shows another snapshot taken at a different location in which a part of the film was intentionally removed. The induced step allowed for the direct comparison between the composite-covered (brighter region on the left) and the bare GCE surface (right). In the latter, a number of bright features with island-type morphology were observed in the vicinities of the induced step. Their closer inspection with higher magnification (red inset) unveiled individual sheets of rGO (of about 2 μm width) loaded with bright clusters of particles with

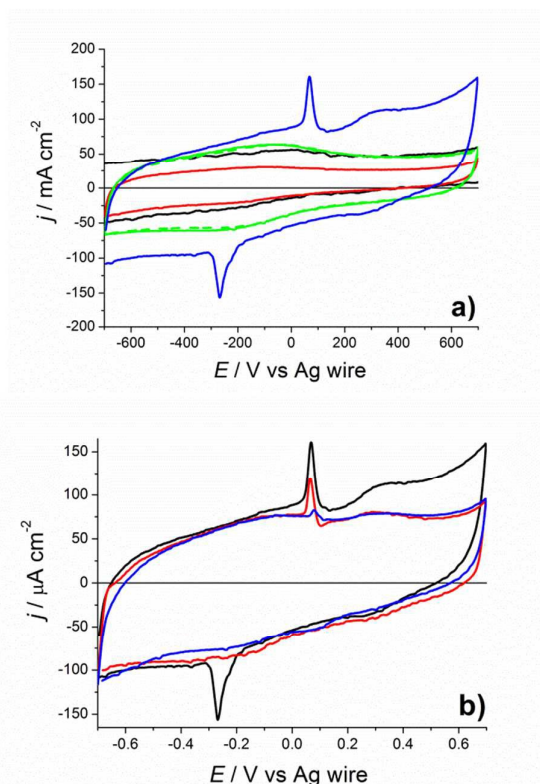


Figure 3. (a) CVs obtained for bare GCE (black solid line), GCE/GOx (red), GCE/Chit95 (green), GCE/Chit95/GOx (green dashed line), and GCE/rGO-Ni NPs (blue) in PBS 0.05 M (pH 7.3). (b) Evolution of the CV for GCE/rGO-Ni NPs (black curve) after its sequential modification to GCE/rGO-Ni/Chit95 (red) and GCE/rGO-Ni/Chit95/GOx (blue). The scan rate was 50 $\text{mV}\cdot\text{s}^{-1}$ in all cases.

size ranging between 20 and 60 nm in (in good agreement with the shape and size of the few-NP aggregates shown in Fig 2b).

An EDS spectrum taken over one of these islands showed that these are mainly composed of carbon, oxygen, and nickel (Fig S3†). The absence of N peaks, allowed discarding the presence of colloidal forms of chitosan. Therefore, the combination of FESEM and EDS support the observation of isolated 2D sheets of rGO-Ni NPs. It might be also concluded that the structure of the composite film consists of a base layer of the rGO-Ni NPs hybrid covered by chitosan hydrogel (which contains the GOx). This structure not only agrees with the changes shown in Fig 3 but also fits the order of assembly followed in the preparation of the composite.

Stability and Catalytic Activity of GOx

The stability of GOx was investigated by testing its catalytic activity in presence of glucose. Figure 5 presents the interrogation tests conducted by CV (panel a) and EIS (panel b) for bare GCE, GCE/GOx, GCE/Chit95/GOx, and GCE/rGO-Ni/Chit95/GOx in 1 mM glucose. Blank measurements in its absence have been also included for comparison purposes. In the absence of glucose, the adsorption of GOx (red solid curve in Fig 5a) resulted in a great blockage of the reversible faradaic processes seen for bare GCE (as also occurred with the capacitive currents in Fig 3a). Accordingly, the anodic peak current density (j_{PA}) dropped by almost $0.5 \text{ mA}\cdot\text{cm}^{-2}$ and ΔE_p grew to 800 mV (see Table 1).

Its corresponding Nyquist plot (red solid curve in Fig 5b) exhibited a semicircle at high-medium frequencies whose diameter was, by far, the largest amongst all the investigated electrodes. In this frequency region, the total impedance is controlled by the apparent charge transfer resistance (R_2) so that, the wider the observed semicircle registered the higher is R_2 .⁵⁴ Agreeing with this qualitative interpretation, R_2 (determined in this case from the fittings to a R_1QR_2 circuit; section S1†) increased by two orders of magnitude ($60.2 \text{ k}\Omega$) since the 583Ω measured for bare GCE. Hence, both the data in Fig 5 and Table 1 indicate that the ET is strongly hindered at the GCE/GOx electrode which, as discussed above, may be due to the poor conformational stability of GOx onto GCE.

As reported for an anodized carbon electrode,⁵⁵ the unfolding of GOx should form a blocking layer on GCE that seriously limits its charge storage capabilities and the ET kinetics. In big contrast, a pair of sharp peaks (and current densities well above those for bare GCE) was observed in the CV of GCE/Chit95/GOx (green solid line). As shown in Table 1, j_{PA} soared to $916 \mu\text{A}\cdot\text{cm}^{-2}$ and ΔE_p fell to 88 mV. In line with this behavior, its Nyquist exhibited a semicircle even narrower than that exhibited by bare GCE. The very low value of R_2 obtained from the fittings, 365Ω , confirmed this view.

Hence, immobilizing GOx on chitosan not only did not block of the ET processes of the $[\text{Fe}(\text{CN})_6]^{3-/4-}$ species but, oppositely, they were slightly favored. The main conclusions are:

(1) When supported on chitosan, the conformational stability of GOx is superior. Chit95 is rich in hydroxyl and amino groups which interact with the hydrophilic residues in the

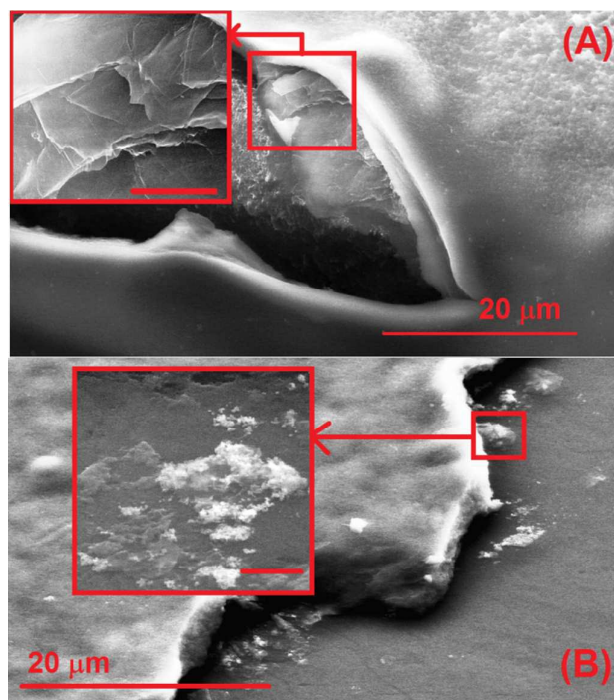


Figure 4. (a, b) FESEM images taken at two different locations over the GCE/rGO-Ni/Chit95/GOx surface. The red insets display areas re-scanned with higher magnification (the width of the red bar is $2 \mu\text{m}$ in both cases).

outer regions of GOx (protein cores are usually hydrophobic) to help keeping the biomolecules in its folded state.^{42,56}

(2) The enhanced redox response is consistent with the enhanced capacitive currents recorded in pure buffer (Fig 3a). As already discussed, the Chit95 matrix may be partially charged so that negatively charged anions and redox probes may be attracted into it and rise their concentrations over those at the bulk electrolyte (thus, explaining the enhanced response).

Although the most important enhancement in the ET occurred after deposition of the Chit95/GOx hydrogel, the incorporation of rGO-Ni NPs sheets at the base of this construct gave a further boost (see insets of Fig 5). Accordingly, j_{PA} and ΔE_p improved to $956 \mu\text{A}\cdot\text{cm}^{-2}$ and 83 mV, respectively. Furthermore, the semicircle diameter followed a concomitant decrease. This was additionally confirmed by a minimum R_2 of 335Ω . Hence, due to the synergies described in the introduction, the GCE/rGO-Ni/Chit95/GOx electrode exhibited the best electroactivity within the investigated series.

Not surprisingly, the response of bare GCE and GCE/GOx was slightly hampered in 1 mM glucose (black and red dashed lines, respectively). Supporting this view, j_{PA} decreased by a 28% (bare GCE) and 14% (GCE/GOx) compared to the response in absence of glucose. In good agreement, R_2 increased by a 360% and 13%, respectively. These results indicate that:

(1) None of these electrodes exhibited apparent catalytic activity towards glucose.

(2) Glucose seemed to induce a partial blockage of the ET.

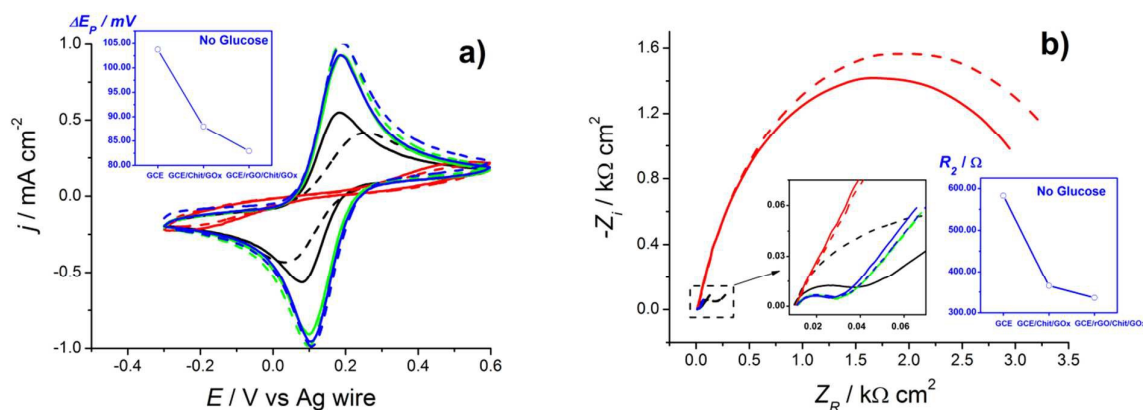


Figure 5. Redox response registered for bare GCE (black), GCE/GOx (red), GCE/Chit95/GOx (green) and GCE/rGO-Ni/Chit95/GOx electrodes (blue) in PBS 0.05 M (pH 7.3) + 2 mM $[\text{Fe}(\text{CN})_6]^{3-/4-}$ + 1 mM D-glucose (dashed lines). The curves in the absence of glucose are also included for comparison (solid lines). (a) CVs recorded at $50 \text{ mV}\cdot\text{s}^{-1}$. (b) Nyquist plots collected at 0.15 V (oscillation amplitude: 10 mV). The black inset features an enlargement of the impedance spectra in the high-medium frequency range. The blue insets display the evolution of ΔE_p and R_2 .

Table 1 Anodic peak current densities (j_{PA}), peak-to-peak potential difference (ΔE_p) and apparent charge transfer resistance (R_2) derived from the responses registered in Figure 5 for GCE/rGO-Ni/Chit95/GOx in the presence and absence of 1 mM glucose.

Electrode	$[\text{G}]/\text{mM}$	$j_{PA}/\text{mA}\cdot\text{cm}^{-2}$	$\Delta E_p/\text{V}$	$R_2/k\Omega$
Bare GCE	0	0.583	104	0.583
GCE/GOx	0	0.104	800	60.2
GCE/Chit95/GOx	0	0.916	88	0.365
GCE/rGO-Ni/Chit95/GOx	0	0.956	83	0.336
Bare GCE	1	0.418	209	2.68
GCE/GOx	1	0.089	800	68.0
GCE/Chit95/GOx	1	1.023	93	0.363
GCE/rGO-Ni/Chit95/GOx	1	1.047	88	0.353

A reasonable hypothesis to explain these results considers the blockage of electroactive sites by glucose molecules. The adsorption of glucose onto carbon materials has been scarcely explored⁵⁷⁻⁵⁸ and, to our best knowledge, nothing has been published about its adsorption on GCE. Then, to check this phenomenon, we took CV and EIS measurements under the same working conditions within a wide range of glucose concentrations $[\text{G}]=0.05\text{--}13 \text{ mM}$ (Fig S1†). By increasing $[\text{G}]$, j_{PA} declined continuously and R_2 followed a concomitant increase. The j_{PA}/R_2 vs $[\text{G}]$ curves clearly resembled to the reported adsorption isotherms of glucose on mesoporous carbons.⁵⁸ From this experiment the maximum coverage of glucose on GCE was estimated to be below half a monolayer ($\theta_G=0.4$).

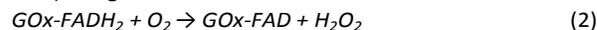
As discussed above, the GCE/GOx electrode must be blocked by a layer of denaturated enzyme so that any additional blocking (due to glucose adsorption) would have a very small impact on the ET (as confirmed in Fig 5). In great contrast with this behavior, the CVs of GCE/Chit95/GOx and GCE/rGO-Ni/Chit95/GOx exhibited enhanced peak currents (green and blue dashed lines in Fig 5a). The integrated anodic

charge (Q_A) increased by a 13% and 15%, respectively, but the values of ΔE_p and R_2 barely changed. The Nyquist plots for both electrodes in absence and presence of glucose virtually overlapped each other. Although no evidence of direct ET from GOx was found (Fig S2†), the consistently enhanced peak currents observed for the GOx-modified electrodes may be attributed to the catalytic activity of the enzyme.

GOx is known to selectively oxidize β -D-glucose to D-glucono-1,5-lactone as follows:



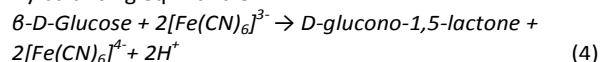
In presence of O_2 , the flavin adenine dinucleotide redox cofactor (FAD, the initial acceptor of two electrons and two protons) is regenerated:



Hydrogen peroxide oxidation, constitutes the detection principle in “first generation” electrochemical biosensors. Alternatively, redox mediators have been used as electron acceptors to reduce their high operating potentials (second generation). In our experiments, the electrolyte contains no O_2 and, thus, the mediator must be the initial electron acceptor:



By balancing eq. 1 and 3:



Therefore, the enzymatic activity of GOx results in an increased concentration of $[\text{Fe}(\text{CN})_6]^{4-}$. As its oxidation to $[\text{Fe}(\text{CN})_6]^{3-}$ occurs at the anodic peak, the activity of the enzyme establishes a feed-back loop due to GOx which results in enhanced oxidation peaks.

Calibration Curves

Encouraged by these results, the GCE/rGO-Ni/Chit95/GOx electrode was further interrogated in a wide range of $[\text{G}]$ (0.025–12 mM). Accordingly, the proof-of-concept experiments were recorded in triplicate (Figs 6, S3†, and S4†). As shown in

Fig 6a, the CVs did not follow great changes in shape. However, the peak currents followed a slight but progressive decrease (red inset). The average j_{PA} vs $[G]$ plot (blue inset) confirmed this view and exhibited two linear domains which were fitted to a couple of straight lines. The widest region, 1–12 mM, covers normal blood glucose levels in healthy humans (3.9–6.5 mM) and most cases of hypo and hyperglycemia in diabetics.

The second is much narrower (0.025–1 mM) but more sensitive (as inferred from its greater slope). The EIS interrogation showed a continuous growth of the semicircle diameter (Fig 6b) upon the increase of $[G]$. Remarkably, two identical linear domains were also spotted in the average R_2 vs $[G]$ plot (blue inset). The quantitative average data in Table 2 confirms both the decline of j_{PA} and the growth of R_2 . Both the CV and EIS calibration is consistent with a progressive hindering of the ET as the amount of glucose is increased.

Electroanalytical Performance and Detection Mechanism

The average sensitivity of the biosensor in the sub-millimolar (S_L) and millimolar (S_H) domains was derived from the slopes of the fitting curves in Fig 6 (Table 3). Under the voltammetric determination, these achieved values of $S_L=68 \mu\text{A}\cdot\text{cm}^{-2}\cdot\text{mM}^{-1}$ and $S_H=6 \mu\text{A}\cdot\text{cm}^{-2}\cdot\text{mM}^{-1}$. These data suggest a superior sensitivity of the biosensor in the sub-millimolar range. While the sensitivity of the individual GCE/rGO-Ni/Chit95/GOx electrodes in the millimolar scale (S_H) were very close to S_H (c.a. 6–7 $\mu\text{A}\cdot\text{cm}^{-2}\cdot\text{mM}^{-1}$), the maximum S_L achieved by the biosensor was about twice the S_L (129 $\mu\text{A}\cdot\text{cm}^{-2}\cdot\text{mM}^{-1}$). In good agreement with these findings, the impedimetric determination showed to be about 15 times more sensitive in the submillimolar domain (Table 3).

The limits of detection (LOD) were evaluated for both methods considering a S/N ratio of 3. Thus, minimum values of 390 and 254 μM were obtained from the voltammetric and impedometric methods, respectively. These results suggest that the impedometric determination is slightly more sensitive. Compared to other enzymatic biosensors based on GOx and graphene-MNPs/SNPs conjugates (e.g. rGO-Cu,²⁷ rGO-TiO₂,³⁰ rGO-Au,²³ GO-Pt,²⁸ and rGO-hydroxyapatite;⁴⁹ 2nd–6th entries in Table 4), the GCE/rGO-Ni/Chit95/GOx electrode exhibited the highest sensitivity (a close performance was only achieved by the GCE/GO-Pt/Chit/GOx sensor).²⁸

The same conclusion was reached by comparison with other biosensors based on GOx and undecorated forms of graphene (rGO;^{43,50} GO;⁵⁹ and graphene nanosheets, GNS;⁶⁰ see Table 4). In fact, the best sensitivity attained by these sensors was 48 $\mu\text{A}\cdot\text{cm}^{-2}\cdot\text{mM}^{-1}$ (GCE/GNS/Nafion/GOx),⁶⁰ which is 20 $\mu\text{A}\cdot\text{cm}^{-2}\cdot\text{mM}^{-1}$ below the average sensitivity demonstrated in our results. Non-enzymatic sensors based on graphene-CuO have also exhibited linear response in the sub-millimolar range and a better combination of LODs and S .^{33,34} The few number of non-enzymatic sensors based on the rGO-Ni NPs hybrid have presented low LODs (0.1–1 μM).^{37–41} On the other hand, while the GCE/rGO-Ni sensors reported by Y. Zhang³⁹ *et al* and Z. Wang⁴¹ *et al* exhibited sensitivities around

$10^3 \mu\text{A}\cdot\text{cm}^{-2}\cdot\text{mM}^{-1}$, the other three were less sensitive than the GCE/rGO-Ni/Chit95/GOx biosensor.

From this broad comparison it is concluded that non-enzymatic graphene-MNPs/SNPs sensors, which are based on different working and detection principles and operate at pHs well above the physiological level, present enhanced electroanalytical performance compared to their enzymatic counterparts. Beyond the good electrocatalytic properties of MNPs/SNPs, the results unavoidably evoke the idea of a still limited stability/loading of enzyme in those systems (further investigation will be required to ascertain this point). In any case, the presented results demonstrate an important improvement in the stability of GOx when supported on Chit95 and, as a result, the achieved sensitivities are amongst the finest reported for glucose biosensors based upon GOx and graphene. In fact, good responsiveness was not only noticed for the lowest $[G]$ studied in these experiments (25 μM), which is close to the detection limit reported for GCE/rGO/Chitosan/GOx (20 μM),⁴³ but even at a much lower $[G]$ of 100 nM as shown in the ESI (Fig S6[†]).

The progressive hindering of the redox response in Fig 6, as opposed to the enhanced current densities evidenced in Fig 5, is a clear indication that the activity of GOx is not the only phenomenon making part of the sensing mechanism. We must recall that the adsorption of glucose on bare GCE was demonstrated in Fig S1[†]. Hence, a hybrid enzymatic/non-enzymatic detection mechanism is proposed to explain the net response in Fig 6. The progressive blockage of uncovered GCE surface sites in presence of increasing amounts of glucose molecules, may counter-balance the enhanced response of the biosensor due to the activity of GOx. Hence, a net deterioration of the ET kinetics is observed in the interrogation tests. Although further research is required to confirm this point, the behavior in Fig 6 is strongly suggested to be controlled by the progressive adsorption of glucose (in fact, the shape of the R_2/j_{PA} vs $[G]$ plots remind a typical two-step adsorption isotherm).

Reproducibility, Stability, and Interference Studies

The errors presented in Table 2, correspond to relative standard deviations (RSD) in the range 4–6%. In good agreement, the RSD of the j_{PA} registered in 1 mM glucose for three electrode samples was 4.9%. Taking into account the variety of synthetic and assembly steps involved in the preparation of the biosensor, these results evidence a good degree of reproducibility. The RSD of five consecutive measurements taken with a freshly prepared electrode fell below 1.3% (see the curves in Fig S7[†]) which indicates an excellent repeatability. The stability of the biosensor towards continuous cycling was judged upon collecting 100 consecutive CVs. Although the j_{PA} followed an important decrease, the biosensor was still operative.

Its durability was evaluated for a period of one month. After 3 weeks storage, a dramatic decrease of the electroactivity was observed (Fig S7[†]). At first glance, the electrode surface looked like cracked and scaly. This evidence suggests that the drying of the hydrogel film results in a great

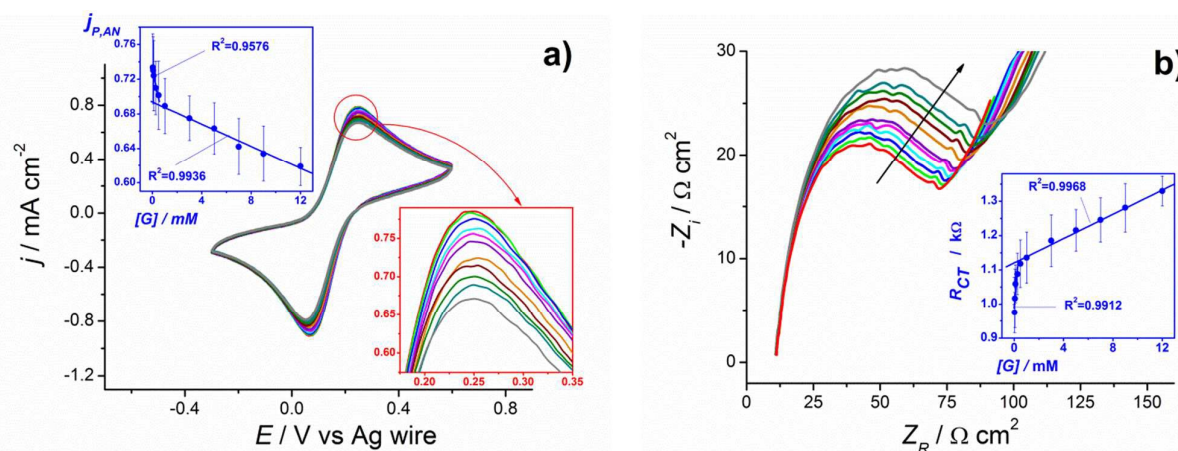


Figure 6. Electrochemical interrogation of the biosensor in the presence of increasing concentrations of glucose $[G]$: 0.025 (red), 0.050 (green), 0.100 (blue), 0.250 (cyan), 0.500 (magenta), 1 (purple), 3 (orange), 5 (wine), 7 (olive), 9 (dark cyan), and 12 mM (grey). **(a)** CVs recorded at $50 \text{ mV}\cdot\text{s}^{-1}$. The changes in the anodic peak are shown with higher detail in the red inset. **(b)** Nyquist plots collected at $+0.15 \text{ V}$ and oscillation amplitude of 10 mV . The average changes in j_{pA} and R_2 for three GCE/rGO-Ni/Chit95/GOx electrodes are shown in the blue insets with the corresponding calibration curves. The error bars represent the standard deviations. The electrolyte was PBS 0.05 M (pH 7.3) + $2 \text{ mM Fe(CN)}_6^{3-/4-}$.

loss of performance (indeed, as also seen in the figure, the situation improved when storage was performed under appropriate conditions of hydration). Ascorbic acid (AA) and uric acid (UA) are some of the most important species interfering in the electrochemical detection of glucose in plasma samples (although ten times more diluted, these oxidize in simultaneous with H_2O_2 in first generation biosensors). To investigate this effect, additional interrogation tests were conducted in PBS 0.05 M + $2 \text{ mM Fe(CN)}_6^{3-/4-}$ + 1 mM glucose after successive additions of AA and UA to concentrations of $50, 75, \text{ and } 100 \mu\text{M}$ (Fig S8†).

The addition of AA, led to total variations in j_{pA} and ΔE_p within the measurement error (1.7% and 1% , respectively) and to negligible changes in the Nyquist plots. Oppositely, UA induced a decrease in j_{pA} of ca. 6.6% and ΔE_p increased more than 10% (the changes in the Nyquist also became more evident as seen in the inset of Fig S8b†). These results indicate that while AA has a negligible effect in the response of the biosensor, UA poses a significant interference which may slightly overestimate the analytical signal. Since the oxidation of AA and UA in bare GCE occurs at $E > 0.35 \text{ V}$ vs Ag/AgCl,⁶¹ competitive adsorption is suggested as a possible interference mechanism.

Conclusions

Sheets of reduced graphene oxide (rGO) decorated with clusters, or isolated NPs, of Ni were synthesized through the one-pot reduction of GO and Ni^{2+} . rGO-Ni/Chit95/GOx nanocomposite films, constituted by a base layer of the conjugate and a GOx-containing chitosan hydrogel on top, were deposited onto a GCE. The interrogation of the modified electrode in dilute glucose solutions demonstrated a significant activity of the enzyme supported on Chit95. Further interrogation in a wider range of $[G]$, demonstrated the

Table 2. Average anodic peak current densities (j_{pA}) and apparent charge transfer resistance (R_2) plotted in the blue insets of Fig 6. The errors correspond to the standard deviation of the three experiments.

$[G] / \text{mM}$	$j_{pA} / \text{mA}\cdot\text{cm}^{-2}$	$R_2 / \text{k}\Omega$
0.025	0.73 ± 0.04	0.97 ± 0.06
0.050	0.73 ± 0.04	1.02 ± 0.09
0.100	0.72 ± 0.04	1.06 ± 0.05
0.250	0.71 ± 0.03	1.09 ± 0.06
0.500	0.70 ± 0.04	1.12 ± 0.07
1.000	0.69 ± 0.03	1.13 ± 0.07
3.000	0.67 ± 0.03	1.18 ± 0.07
5.000	0.66 ± 0.03	1.21 ± 0.06
7.000	0.64 ± 0.03	1.24 ± 0.06
9.000	0.63 ± 0.03	1.28 ± 0.07
12.00	0.62 ± 0.02	1.33 ± 0.04

Table 3. Parameters obtained by fitting the average data in the blue insets of Fig 6 to straight lines defined by the equation $Y = A + S \cdot [G]$, with Y being j_{pA} and R_2 , A the y-intercept, and S the slope.

Mode	$[G] / \text{mM}$	$S / \mu\text{A}\cdot\text{cm}^{-2}\cdot\text{mM}^{-1}$	$A / \mu\text{A}\cdot\text{cm}^{-2}$	R^2
CV	0.025-1	68	732	0.958
CV	1-12	6	694	0.994
	$[G] / \text{mM}$	$S / \Omega\cdot\text{mM}^{-1}$	A / Ω	R^2
EIS	0.025-1	262	1004	0.925
EIS	1-12	17	1121	0.997

feasibility of the system as a second generation electrochemical biosensor with good linearity found in the millimolar and sub-millimolar scales (both under voltammetric and impedimetric mode). Good reproducibility and short-term repeatability upon consecutive measurements were also demonstrated. Tests in presence of AA and UA showed a negligible effect of the first and a small (and likely manageable) interference of the latter in the response of the biosensor. The stability towards continuous cycling and storage under dry conditions were limited.

Analyst

PAPER

Table 4. Sensitivity (*S*), limit of detection (*LOD*), and linear dynamic range (*LDR*) reported in the literature for the electrochemical detection of glucose using different graphene-based sensors.

Sensor	Type	Method	<i>S</i>	<i>LOD</i> /μM	<i>LDR</i> /mM	Ref.
GCE/rGO-Ni/Chitosan/GOx	E ^u	CV	129 μA·cm ⁻² ·mM ⁻¹	390	0.025-1	This work
		EIS	497 Ω·mM ⁻¹	254		
GCE/rGO-Cu/Nafion/GOx	E	CV	34 μA·cm ⁻² ·mM ⁻¹	5.00	0.05-12	[27]
GCE/rGO-TiO ₂ /Nafion/GOx	E	CV	6 μA·cm ⁻² ·mM ⁻¹	–	Up to 8	[30]
GCE/rGO-Hap ^u /GOx	E	CV	17 μA·cm ⁻² ·mM ⁻¹	30.0	0.1-11	[49]
GCE/GO-Pt/Chitosan/GOx	E	CA ^c	113 μA·cm ⁻² ·mM ⁻¹	0.6	0.001-2.25	[28]
Au/rGO-Au/Chitosan/GOx	E	CV	0.55 μA·mM ⁻¹	180	2.0-10	[23]
GCE/rGO/Chitosan/GOx	E	CV	38 μA·cm ⁻² ·mM ⁻¹	20.0	0.08-12	[43]
GCE/rGO/GOx	E	CA	1.85 μA·cm ⁻² ·mM ⁻¹	–	0.1-27	[50]
GCE/GNS ^u /Nafion/GOx	E	CV	48 μA·cm ⁻² ·mM ⁻¹	–	0.2-1.4	[60]
Pt/GO/GOx	E	CA	8 μA·cm ⁻² ·mM ⁻¹	–	0.1-20	[59]
CPE ^e /rGO-Ni	NE ^J	CA	1.1 μA·cm ⁻² ·mM ⁻¹	0.47	0.001-1	[37]
AER ^u /rGO-Ni	NE	CA	82 μA·cm ⁻² ·mM ⁻¹	1.05	0.001-1	[38]
GCE/rGO-Ni	NE	CA	1020 μA·cm ⁻² ·mM ⁻¹	0.1	0.002-2.1	[39]
GCE/rGO/PANI ^h /Ni	NE	CA	30 μA·cm ⁻² ·mM ⁻¹	0.1	0.0001-1	[40]
GCE/rGO-Ni	NE	CA	813 μA·cm ⁻² ·mM ⁻¹	–	0.001-0.110	[41]
GCE/rGO-CuO	NE	CA	2221 μA·cm ⁻² ·mM ⁻¹	0.1	0.0004-3	[33]
GCE/SG ⁱ -CuO	NE	CA	1299 μA·cm ⁻² ·mM ⁻¹	0.08	0.1-10.5	[34]

^a Enzymatic; ^b Hydroxyapatite; ^c Chronoamperometry; ^d Graphene Nanosheets; ^e Carbon Paste Electrode; ^f Non-enzymatic; ^g Anion Exchange Resin Microspheres; ^h Polyaniline; ⁱ Sulfur-Doped Graphene

In addition to the lower cost and toxicity of Ni, other advantages include its low operating potential and superior sensitivity in the submillimolar range (compared to other reported glucose biosensor based on GOx and graphene-MNPs/SNPs). The demonstrated performance is well suited for most of the practical applications of a disposable glucose sensor (regular self-management tasks or early detection of hypoglycemia peaks) and suggests potential applications in the development of non-invasive assays based on more accessible human sera such as saliva or tears

Acknowledgements

This work was supported by the European Union (FEDER) and National funds through programmes COMPETE and POPH (Pest-C/EQB/LA0006/2013 and PTDC/EME-MFE/103051). R.K., P. M. V. F., and J. M. C. acknowledge the FCT (Fundação para a Ciência e a Tecnologia de Portugal) for the concession of doctoral and post-doctoral grants (SFRH/BD/80105/2011, SFRH/BD/111274/2015, and SFRH/BPD/75259/2010).

Notes and references

Author Contributions

E.T., A.F.S., and J.V. conceived the project. R.K. synthesized and characterized the conjugate. J.M.C. and P.M.V.F. fabricated and

characterized the biosensor. R.K., J.V., E.T., J.M.C., and A.F.S., analyzed the results. J.M.C. wrote the paper.

- 1 S. Wild, G. Roglic, A. Green, R. Sicree and H. King, *Diabetes Care*, 2004, **27**, 1047.
- 2 R. R. Holman, S. K. Paul, M. A. Bethel, D. R. Matthews and H. A. Neal, *N. Engl. J. Med.*, 2008, **359**, 1577.
- 3 J. Wang, *Chem. Rev.*, 2008, **108**, 814.
- 4 B. Hock, *Anal. Chim. Acta*, 1997, **347**, 177.
- 5 E. Katz and I. Willner, *Electroanalysis*, 2003, **15**, 913.
- 6 K. Haupt and K. Mosbach, *Chem. Rev.*, 2000, **100**, 2495.
- 7 Press Release by Persistence Market Research Pvt. Ltd., 2014, New York City; <http://www.persistencemarketresearch.com/mediarelease/biosensor-market.asp>
- 8 J. Wang, *Biosens. Bioelectron.*, 2006, **21**, 1887.
- 9 M. Rabe, D. Verdes and S. Seeger, *Adv. Colloid Interface Sci.*, 2011, **162**, 87.
- 10 F. W. Scheller, F. Schubert, B. Neumann, D. Pfeiffer, R. Hintsche, I. Dransfeld, U. Wollenberger, R. Renneberg, A. Warsinke, G. Johansson, M. Skoog, X. Yang, V. Bogdanovskaya, A. Bückmann and S. Y. Zaitsev, *Biosens. Bioelectron.*, 1991, **6**, 245.
- 11 B. D. Malhotra, A. Chaubey and S. P. Singh, *Anal. Chim. Acta*, 2006, **578**, 59.
- 12 X. L. Luo, A. Morrin, A. J. Killard, and M. R. Smyth, *Electroanalysis*, 2006, **18**, 319.
- 13 J. Liu, A. Chou, W. Rahmat, M. N. Paddon-Row and J. J. Gooding, *Electroanalysis*, 2005, **17**, 38.

- 14 K. S. Novoselov, D. Jiang, F. Schedin, T. J. Booth, V. V. Khotkevich, S. V. Morozov and A. K. Geim, *Proc. Natl. Acad. Sci. USA*, 2005, **102**, 10451.
- 15 A. Reina, X. Jia, J. Ho, D. Nezich, H. Son, V. Bulovic, M. S. Dresselhaus and J. Kong, *Nano Lett.*, 2009, **9**, 30.
- 16 M. Pumera, *Mater. Today*, 2011, **14**, 308.
- 17 A. Bonanni, A. H. Loo and M. Pumera, *TRAC-Trend Anal. Chem.*, 2012, **37**, 12.
- 18 Y. B. Zhang, Y. W. Tan, H. L. Stormer and P. Kim, *Nature*, 2005, **438**, 201.
- 19 R. K. Joshi, S. Alwarappan, M. Yoshimura, V. Sahajwalla, and Y. Nishina, *Appl. Mater. Today*, 2015, **1**, 1.
- 20 H. Fan, L. Wang, K. Zhao, N. Li, Z. Shi, Z. Ge, and Z. Jin, *Biomacromolecules*, 2010, **11**, 2345.
- 21 T. J. Davies, M. E. Hyde and R. G. Compton, *Angew. Chem. Int. Ed.*, 2005, **44**, 5121.
- 22 C. Gómez-Navarro, J. C. Meyer, R. S. Sundaram, A. Chuvilin, S. Kurasch, M. Burghard, K. Kern and U. Kaiser, *Nano Lett.*, 2010, **10**, 1144.
- 23 C. Shan, H. Yang, D. Han, Q. Zhang, A. Ivaska and L. Niu, *Biosens. Bioelectron.*, 2010, **25**, 1070.
- 24 P. T. Yin, T-H. Kim, J-W. Choi and K-B. Lee, *Phys. Chem. Chem. Phys.*, 2013, **15**, 12785.
- 25 K. Turcheniuk, R. Boukherroub and S. Szunerits, *J. Mat. Chem. B*, 2015, **3**, 4301.
- 26 K. Zhang, *Appl. Surf. Sci.*, 2012, **258**, 7327.
- 27 K-J. Huang, L. Wang, J. Li, T. Gan and Y-M. Liu, *Measurement*, 2013, **46**, 378.
- 28 H. Wu, J. Wang, X. Kang, C. Wang, D. Wang, J. Liu, I. A. Aksay and Y. Lin, *Talanta*, 2009, **80**, 403.
- 29 Y-T. Xu, Y. Guo, C. Li, X-Y. Zhou, M. C. Tucker, X-Z. Fu, R. Sun and C-P. Wong, *Nano Energy*, 2015, **11**, 38.
- 30 H. D. Jang, S. K. Kim, H. Chang, K-M. Roh, J-W. Choi and J. Huang, *Biosens. Bioelectron.*, 2012, **38**, 184.
- 31 X. Huo, J. Liu, B. Wang, H. Zhang, Z. Yang, X. She and P. Xi, *J. Mat. Chem. A*, 2013, **1**, 651.
- 32 Y. Ma, M. Zhao, B. Cai, W. Wang, Z. Ye and J. Huang, *Chem. Commun.*, 2014, **50**, 11135.
- 33 X. Wang, E. Liu and X. Zhang, *Electrochim. Acta*, 2014, **130**, 253.
- 34 Y. Tian, Y. Liu, W-P. Wang, X. Zhang and W. Peng, *Electrochim. Acta*, 2015, **156**, 244.
- 35 Q. Bao, D. Zhang and P. Qi, *J. Colloid Interface Sci.*, 2011, **360**, 463.
- 36 M. B. Gholivand, M. Khodadadian and M. Omid, *Mater. Sci. Eng. C Mater. Biol. Appl.*, 2013, **33**, 774.
- 37 W. Qu, L. Zhang and G. Chen, *Biosens. Bioelectron.*, 2013, **42**, 430.
- 38 R. Zhang, S. Lu, L. Zhang and G. Chen, *J. Chromatogr. A*, 2014, **1374**, 261.
- 39 Y. Zhang, X. Xiao, Y. Sun, Y. Shi, H. Dai, P. Ni, J. Hu, Z. Li, Y. Song, and L. Wang, *Electroanalysis*, 2013, **25**, 959.
- 40 B. Zhang, Y. He, B. Liu, D. Tang, *Microchim. Acta*, 2015, **182**, 625.
- 41 Z. Wang, Y. Hu, W. Yang, M. Zhou, and X. Hu, *Sensors*, 2012, **12**, 4860.
- 42 B. J. Li and H. Q. Cao, *J. Mater. Chem.*, 2011, **21**, 3346.
- 43 X. Kang, J. Wang, H. Wu, I. A. Aksay, J. Liu and Y. Lin, *Biosens. Bioelectron.*, 2009, **25**, 901.
- 44 J. Borges, J. M. Campiña, H. K. S. Souza, M. P. Gonçalves and A. F. Silva, *Soft Matter*, 2012, **8**, 1190.
- 45 J. Borges, J. M. Campiña and A. F. Silva, *J. Mat. Chem. B*, 2013, **1**, 500.
- 46 H. Qi, C. Wang and N. Cheng, *Microchim. Acta*, 2010, **170**, 33.
- 47 M. K. Patel, M. A. Ali, S. Srivastava, V. V. Agrawal, S. G. Ansari and B. D. Malhotra, *Biosens. Bioelectron.*, 2013, **50**, 406.
- 48 R. Krishna, E. Titus, L. C. Costa, J. C. J. M. D. S. Menezes, M. R. P. Correia, S. Pinto, J. Ventura, J. P. Araújo, J. A. S. Cavaleiro and J. J. A. Gracio, *J. Mater. Chem.*, 2012, **22**, 10457.
- 49 G. Bharath, R. Madhu, S-M. Chen, V. Veermani, A. Balamurugan, D. Mangalaraj and N. Ponpandian, *J. Mater. Chem. B*, 2015, **3**, 1360.
- 50 B. Unnikrishnan, S. Palanisamy and S-M. Chen, *Biosens. Bioelectron.*, 2013, **39**, 70.
- 51 C. Mattevi, G. Eda, S. Agnoli, S. Miller, K. A. Mkhoyan, O. Celik, D. Mastrogiovanni, G. Granozzi, E. Garfunkel and M. Chhowalla, *Adv. Funct. Mater.*, 2009, **19**, 2577.
- 52 M. Acik, G. Lee, C. Mattevi, M. Chhowalla, K. Cho and Y. J. Chabal, *Nature Mater.*, 2010, **9**, 840.
- 53 Q. Z. Wang, X. G. Chen, N. Liu, S. X. Wang, C. S. Liu, X. H. Meng and C. G. Liu, *Carbohydr. Polym.*, 2006, **65**, 194.
- 54 J. M. Campiña, A. Martins and F. Silva, *J. Phys. Chem. C*, 2007, **111**, 5351.
- 55 Q. Chi, J. Zhan, S. Dong and E. Wang, *Electrochim. Acta*, 1994, **39**, 2431.
- 56 J. Borges, J. M. Campiña and A. F. Silva, *J. Phys. Chem. B*, 2013, **117**, 16565.
- 57 T. L. Blaney, O. Lindan, and R. E. Sparks, *Trans. Amer. Soc. Artif. Int. Organs*, 1966, **12**, 7.
- 58 P-W. Chung, A. Charmot, O. M. Gazit, and A. Katz, *Langmuir*, 2012, **28**, 15222.
- 59 Y. Liu, D. Yu, C. Zeng, Z. Miao and L. Dai, *Langmuir*, 2010, **26**, 6158.
- 60 C. Fu, W. Yang, X. Chen and D. G. Evans, *Electrochem. Commun.*, 2009, **11**, 997.
- 61 M. A. Kamyabi and M. A. Shafiee, *J. Braz. Chem. Soc.*, 2012, **23**, 593.